Metastable spin-phase diagrams in antiferromagnetic Bose-Einstein condensates

E. Serrano-Ensástiga [*] and F. Mireles [†]

Departamento de Física, Centro de Nanociencias y Nanotecnología, Universidad Nacional Autónoma de México, Apdo. Postal 14, 22800 Ensenada, Baja California, México

(Received 5 September 2021; revised 26 October 2021; accepted 29 November 2021; published 13 December 2021)

Spinor Bose-Einstein condensates under external magnetic fields exhibit well-characterized spin domains of its ground state due to spin-dependent interactions. At low temperatures, collision-induced spin-mixing instabilities may promote the condensate to dwell into metastable states occurring near the phase boundaries. In this paper, we study theoretically the metastable spin-phase diagram of a spin-1 antiferromagnetic Bose-Einstein condensate at zero and finite temperatures. The approach makes use of Hartree-Fock theory and exploits the symmetry of the Hamiltonian and of the order parameters yielding a closed system of transcendental equations for the free energy, fully avoiding the use of self-consistency methods. Our results are consistent with recent experiments and allow us to explain qualitatively the different types of observed quench dynamics. In addition, we found that similar phenomena should occur in antiferromagnetic spinor condensates with a sudden change in the temperature. It is shown also that the increase in temperature induces a traceable shift of the ferromagnetic-polar transition boundary, behavior previously not noted by self-consistent mean-field calculations.

DOI: 10.1103/PhysRevA.104.063308

I. INTRODUCTION

Spinor Bose-Einstein condensates (BECs) of ultracold atoms can be manipulated nowadays with astonishing precision offering unprecedented opportunities to study spin-dependent many-body physics [1–3]. Of crucial importance is the underlying physics of the phase diagram in spinor BECs where the nature of the spin domain phases strongly depends on the atomic species and on the external fields. The study of the spin-phase diagram in spinor BECs via mean-field theories were introduced first for spin $f = 1$ [4,5] and, subsequently, for higher spins ($f = 2$–4, 6, 8) [1,6–9] where the usual parameters of the phase diagram are the coupling factors of the different spin-dependent interactions and/or the coefficients of the linear and quadratic Zeeman interactions. The predicted phase diagrams have been confirmed for spin-1 BECs with antiferromagnetic (^{23}Na [10–12]) and ferromagnetic spin-dependent interactions (^{87}Rb [13] and ^{7}Li [14]) to mention a few.

It is known that in spinor BECs, there may occur the coexistence of several domain phases in which its different spin states and associated order parameters are not continuously transformed at the phase boundary leading to a first-order transition. Owing to the noncontinuity of the order parameters, both phases may remain stable, whereas the ground state is given by the lowest-energy state. Consequently, near the phase boundaries may exist metastable phases [15–22] which play a crucial role in a variety of phenomena, such as quantum tunneling [23,24], domain formations [25,26], and quench dynamics [27–29], among others [30,31]. In particular, recent experiments have reported the observation of dynamical quantum phase transitions under different types of quench dynamics in an antiferromagnetic spinor BEC [29], including a more recent experiment that involves a phase transition between excited states [32]. A dynamical phase transition refers to a nonanalytical change in the quench dynamics of the condensate [33], occurring by the sudden change in the controlling parameters that modifies the free energy and stability of each spin phase. Under this perspective, the different quench processes and the existence of dynamical phase transitions can also be understood through the analysis of its corresponding metastable spin-phase diagram.

In this paper, we analyze within Hartree-Fock (HF) theory the emergence of metastable spin domains in a spin-1 antiferromagnetic condensate at finite temperatures. The resulting phase diagrams offer further insights of the nature of the different quench processes observed in Ref. [29]. Our approach starts with the HF approximation [34–36] but take advantage of the common symmetries between the Hamiltonian and the order parameter of the condensate to then reduce the problem to the solution of a system of algebraic-transcendental equations instead to appeal self-consistency. This framework leads us to closed expressions for the study of the metastable phase diagrams and their physical properties, including analytical expressions at low temperatures. The formalism is quite general and can be applied for a spinor condensate of any spin value and any spin-dependent interaction in mean-field theory.

We show the appearance of overlapping regions of the spin domains which tend to increase as the temperature is increased. This allows us to infer similar quench processes due to a sudden change in the temperature, instead of an abrupt change in an external field as performed experimentally in Ref. [29]. We characterize the spin phases in the overlapping regions through calculations of the spin magnetization and the

[*] edensastiga@ens.cnyn.unam.mx
[†] fmireles@cnyn.unam.mx

atom fraction in the magnetic sublevels in order to further distinguish the spin domains among each other. We also uncover a sizable shift of the ferromagnetic-polar (FM-P) phase boundary driven by temperature, in sharp contrast with earlier self-consistent HF results that predicts a fixed phase boundary with temperature [36]. Moreover, the approach enables us to extract a useful analytical approximation of the FM-P phase boundary valid for a wide range of temperatures.

II. MODEL

Let us consider a dilute $f = 1$ spinor Bose-Einstein gas confined in an optical trap with potential $U(\boldsymbol{r})$, and subject to linear (p) and quadratic (q) Zeeman fields oriented along the z axis. The coefficients (q, p) depend explicitly on external fields [1],

$$p = -g\mu_B B, \qquad q = q_B + q_{\mathrm{MW}}, \tag{1}$$

where g is the Landé hyperfine g factor, μ_B is the Bohr magneton, and B is the strength of the external magnetic field. Note that the coefficient q is contributed by the external magnetic-field q_B and from a microwave (MW) field q_{MW}. Hence, the parameters (q, p) can be manipulated independently in a laboratory [37,38], and here they will be our parameters in the phase diagram. We restrict ourselves to $p \geqslant 0$ values because the phase diagram is symmetric by inversion $p \to -p$ [1]. The system is assumed to be weakly interacting and sufficiently diluted such that only two-body collisions are predominant and the s-wave approximation is still valid. The full Hamiltonian of the atomic gas, constituted by the single-particle and interaction terms, is written in the second-quantization formalism as [1,3]

$$\hat{H} = \int \Bigg\{ \hat{\boldsymbol{\Psi}}^\dagger \big(h_s \mathbb{1}_3 - pF_z + qF_z^2\big)\hat{\boldsymbol{\Psi}} + \frac{c_0}{2}\sum_{i,j} \hat{\psi}_i^\dagger \hat{\psi}_j^\dagger \hat{\psi}_j \hat{\psi}_i + \frac{c_1}{2}\sum_{\alpha,i,j,k,l} (F_\alpha)_{ij}(F_\alpha)_{kl}\hat{\psi}_i^\dagger \hat{\psi}_k^\dagger \hat{\psi}_l \hat{\psi}_j \Bigg\} d\boldsymbol{r}, \tag{2}$$

where $h_s = -\hbar^2\nabla^2/2M + U(\boldsymbol{r})$ is the spatial Hamiltonian. The $\mathbb{1}_3$ is the 3×3 identity matrix, and F_αs are the angular momentum matrices of spin $f = 1$ with $\alpha = x$, y, or z and scaled by $\hbar$, then the F_α matrices are dimensionless. The spinor-quantum field associated with the spinor condensate is denoted by $\hat{\boldsymbol{\Psi}} = (\hat{\psi}_1, \hat{\psi}_0, \hat{\psi}_{-1})^T$, where $\hat{\psi}_m$s are the field operators with $m = -1, 0, 1$ as the possible magnetic quantum numbers, and T denotes the transpose. From now on, we will employ bold Greek symbols for the 1-spinors and bold Latin symbols for the three-dimensional vectors in real space. The Hamiltonian (2) has a symmetry group isomorphic to $SO(2) \times \mathbb{Z}_2$, constituted by the rotations about the z axis and the reflection across the yz plane. The spin-independent and spin-dependent coupling factors c_0 and c_1, respectively, are related to the s-wave scattering lengths a_0 and a_2 of the total spin-F channel a_F ($F = 0, 2$) [4,5],

$$c_0 = \frac{4\pi\hbar^2(a_0 + 2a_2)}{3M}, \qquad c_1 = \frac{4\pi\hbar^2(a_2 - a_0)}{3M}, \tag{3}$$

where M is the atomic mass. Experimental measurements indicate that ^{23}Na atoms have $a_0 = 47.36(80)a_B$ and $a_2 = 52.98(40)a_B$ [1,39] with a_B as the Bohr radius, yielding a BEC with antiferromagnetic interactions ($c_1 > 0$). Our theoretical calculations will be based on a BEC of ^{23}Na atoms for which the values of the coupling factors are $c_0/a_B^3 = 0.42$ eV and $c_1 = c_0/27$, derived with scattering lengths a_F within the quoted experimental values and their uncertainties. Other species could present ferromagnetic interactions ($c_1 < 0$) as ^{87}Rb [13] and ^{7}Li [14].

Mean-field approximation at zero temperature ($T = 0$) assumes that all the atoms in the spinor condensate are in the same quantum state described by an spinor order-parameter $\langle\hat{\boldsymbol{\Psi}}\rangle = \boldsymbol{\Phi}$ [1,3]. The ground-state $\boldsymbol{\Phi} = (\phi_1, \phi_0, \phi_{-1})^T$ of the BEC minimizes the functional mean-field energy $E[\boldsymbol{\Phi}] = \langle\hat{H}\rangle$. We will consider the uniform case with $U(\boldsymbol{r}) = 0$ and, hence, the ground-state $\phi_j(\boldsymbol{r}) = \phi_j e^{i\boldsymbol{k}\cdot\boldsymbol{r}}$ with $\boldsymbol{k} = \boldsymbol{0}$. $E[\boldsymbol{\Phi}]$ constrained to a fixed number of particles $N = \boldsymbol{\Phi}^\dagger\boldsymbol{\Phi}$ is reduced to

$$E[\boldsymbol{\Phi}] = \boldsymbol{\Phi}^\dagger\big(-pF_z + qF_z^2\big)\boldsymbol{\Phi} + \frac{c_0}{2}(\boldsymbol{\Phi}^\dagger\boldsymbol{\Phi})^2 + \frac{c_1}{2}\sum_\alpha (\boldsymbol{\Phi}^\dagger F_\alpha \boldsymbol{\Phi})^2 - \mu(\boldsymbol{\Phi}^\dagger\boldsymbol{\Phi} - N), \tag{4}$$

where μ is the chemical potential, i.e., the required energy to add an atom to the condensate. The conditions $\delta E[\boldsymbol{\Phi}]/\delta\phi_m^* = 0$ yield the so-called multicomponent Gross-Pitaevskii (GP) equations. For spin-1 we have five solutions of the GP equations [1,10], identified through the spinor order-parameter $\boldsymbol{\Phi}$. Here we only scrutinize the solutions for the antiferromagnetic cases $c_1 > 0$ and $p \geqslant 0$, which leads to the following phases of the spin-1 BEC:

(1) Ferromagnetic (FM) phase: The spinor order parameter is equal to $\boldsymbol{\Phi} = \sqrt{N}(1, 0, 0)^T$. It is symmetric under rotations about the z axis, imposing that the symmetry group is isomorphic to the special orthogonal group $SO(2)$. Each atom is fully magnetized along the z axis, $M_z \equiv \langle F_z\rangle/N = 1$, and $M_\perp \equiv (\langle F_x\rangle^2 + \langle F_y\rangle^2)^{1/2}/N = 0$, where M_z and $M_\perp$ are dimensionless quantities.

(2) Polar (P) phase: Here $\boldsymbol{\Phi} = \sqrt{N}(0, 1, 0)^T$. Its symmetry group, which is isomorphic to $SO(2) \times \mathbb{Z}_2 \cong O(2)$, consists of rotations about the z axis and time-reversal symmetry (equivalent to an inversion through the origin) [40]. It has zero magnetization $M_z = M_\perp = 0$.

(3) Antiferromagnetic (AF) phase: It consists of a family of quantum states $\boldsymbol{\Phi} = \sqrt{N}(\cos\chi, 0, \sin\chi)^T$ with $\chi \in (0, \pi/4]$. A family of states that represents a phase are also called noninert states [41]. The whole set is symmetric over two geometric operations, a rotation by π about the z axis, and a reflection across the yz plane, implying that the symmetry group is isomorphic to $\mathbb{Z}_2 \times \mathbb{Z}_2$. Note that the AF phase tends to the FM phase when $\chi \to 0$. On the other hand, the AF phase tends to the P phase but oriented over the y axis when $\chi \to \pi/4$. The magnetic moment depends on χ, $M_z = \cos(2\chi)$ and $M_\perp = 0$.

The FM and P phases exist according to mean-field theory for each (q, p) value. On the other hand, the AF phase satisfies [1]

$$\cos\chi = \sqrt{\frac{c_1 N + p}{2c_1 N}}, \tag{5}$$

which implies that the AF phase does not exist for $p > c_1 N$. The limit case $p = c_1 N$ saturates the spin magnetization of the AF phase $M_z = 1$. The phase diagram in the case for zero temperature ($T = 0$) is amenable to analytic results, plotted in Fig. 1 [10]. The ground state for each (q, p) point is the one that minimizes (4). The region of each phase is labeled by FM, P, and AF and painted by a primary color, blue (upper left), red (right), and yellow (lower left), respectively. The solid lines delimit the phase transitions.

The HF approximation [34–36] which, despite being the simplest many-body theory after the mean-field approximation, is known to capture the main relevant physics occurring in the phase diagram and its concomitant boundary regions. Moreover, it allows us to study the spinor condensates at finite temperatures [42]. Formally, in the HF approximation the field operator is given by the order parameter and a perturbation $\hat{\delta}_j$, i.e., $\hat{\psi}_j = \phi_j + \hat{\delta}_j$. For simplicity, we neglect the three-field correlations $\langle \hat{\delta}_i \hat{\delta}_j \hat{\delta}_k^\dagger \rangle$ (Hartree-Fock-Bogoliubov approximation) and the anomalous density $\langle \hat{\delta}_i \hat{\delta}_j \rangle$ (Popov approximation) [35], which gives a reasonable first approximation for diluted gases at all temperatures below the critical temperature [43,44]. Moreover, it has been shown in Refs. [36,45] that the anomalous density does not affect quantitatively the results for a spin-1 ^{87}Rb condensate with the notable exception of the $T \to 0$ limit because of the ratio between the interaction factors $c_0/|c_1| \approx 200$. In our case with ^{23}Na atoms, $c_0/c_1 = 27$ and, hence, the contribution of the anomalous density at zero temperature is significantly reduced. We now apply the elements of the HF theory following Ref. [36] with slight changes in the notation.

The condensate (c) and noncondensate (nc) atoms are represented by a density matrix $\rho^c_{ij} = N^c \phi^*_j \phi_i$ and $\rho^{nc}_{ij} = \langle \hat{\delta}^\dagger_j \hat{\delta}_i \rangle$, respectively. The trace of each density matrix is equal to the number of atoms of each part $\mathrm{Tr}(\rho^a) = N^a$ for $a = n, nc$. The noncondensate atoms ρ^{nc} act as a cloud of atoms thermally excited that interacts nontrivially with the condensate fraction ρ^c. The total system is then denoted by $\rho = \rho^c + \rho^{nc}$ with $\mathrm{Tr}\,\rho = N = N^c + N^{nc}$. Hence, the HF energy with its Lagrange multiplier $\mu(N - \mathrm{Tr}\,\rho)$ is given by

$$E_{\mathrm{HF}} = E_s + \mathrm{Tr}\big[\rho\big(-pF_z + qF_z^2\big)\big] - \mu(\mathrm{Tr}\,\rho - N) + \frac{c_0}{2}\{N^2 + \mathrm{Tr}[\rho^{nc}(2\rho^c + \rho^{nc})]\} + \frac{c_1}{2}\sum_\alpha \{\mathrm{Tr}[\rho F_\alpha]^2 + \mathrm{Tr}[F_\alpha \rho^{nc} F_\alpha (2\rho^c + \rho^{nc})]\}, \tag{6}$$

where the trace involves a summation over the spatial and spinor quantum numbers. For $U(\boldsymbol{r}) = 0$, E_s is the kinetic energy, and then, the spatial quantum number is the wave-vector $\boldsymbol{k}$. The two-body interactions have two terms, the direct and the exchange interactions. The effect of each term over the spin coherence and the distribution of the atoms in the magnetic sublevels is discussed in Ref. [36].

The condensate fraction of the system $\rho^c = N^c \boldsymbol{\Phi}\boldsymbol{\Phi}^\dagger$ is a pure state with $\boldsymbol{k} = \boldsymbol{0}$. Hence, the resulting GP equations $\delta E_{\mathrm{HF}}/\delta \phi^*_m = 0$ are given by a system of three (nonlinear) equations involving ϕ_m and ρ^{nc}. On the other hand, ρ^{nc} is written as a sum of its eigenvectors $\boldsymbol{\xi}^\lambda = (\xi^\lambda_1, \xi^\lambda_0, \xi^\lambda_{-1})^T$

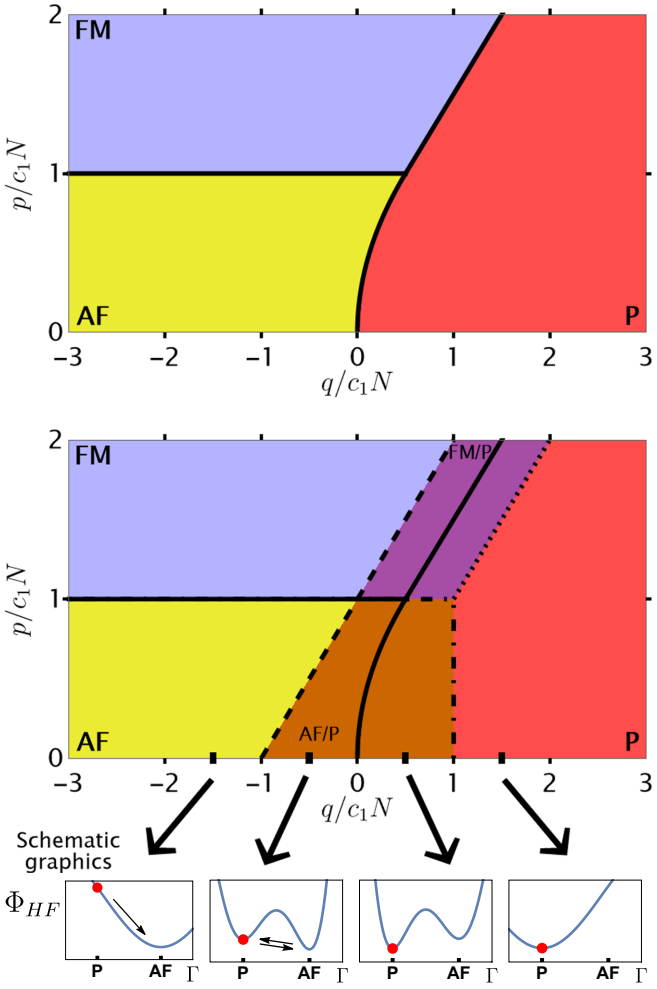

FIG. 1. Top: Ground-state spin-phase diagram of the spin-1 BEC gas at $T = 0$, obtained either by the mean-field approximation [1] or by the HF theory. The FM, P, and AF phases are denoted by a primary color, blue (upper left), red (right), and yellow (lower left), respectively. The solid lines define the phase transitions, and the region of each phase is, respectively, labeled. Center: Metastable spin-phase diagram of the spinor condensate at $T = 0$ calculated with the HF theory and the approach described in Sec. III. The overlaps between the phases FM and P, and AF and P, are denoted by their respective secondary colors purple (upper-center) and orange (lower-center). The boundaries of the admissible region of each phase are indicated by dotted (FM), dashed (P), and dashed-dot (AF) lines, respectively. The lower (upper) boundary of the admissible region of the FM (AF) phase coincides with the solid line that delimits the phase transition. Bottom: Schematic graphics of the thermodynamic potential Φ_{HF} (14) versus an order-parameter variable of ρ^c or ρ^{nc}, included in the set $\Gamma = \{\phi_m, \rho^{nc}_{ij}\}$ for $(q, p) = (n, 0)c_1 N$ with $n = -1.5, -0.5, 0.5, 1.5$, respectively. The (red) point in the graph indicates the initial state of the spinor condensate (P phase), and the arrows denote the phase transition via quantum tunneling or by the presence of an effective force

weighted by their Bose-Einstein distribution factor n_λ,

$$\rho^{nc}_{ij} = \sum_\lambda n_\lambda \xi^\lambda_i \xi^{\lambda *}_j, \qquad n_\lambda = (e^{\beta \epsilon_\lambda} - 1)^{-1}. \tag{7}$$

The global subindex λ includes the spatial and spinor quantum numbers $\lambda = (\boldsymbol{k}, \nu)$ with $\nu = 1$–3 and $\beta = 1/k_B T$ where k_B is the Boltzmann constant. The eigenvectors $\boldsymbol{\xi}^{\lambda}$ and their associated energies ϵ_λ are obtained by the noncondensate Hamiltonian A, given by $A_{ij} = \delta E_{\rm HF}/\delta \rho^{nc}_{ji}$. The decoupling of the spatial and spinor parts in the Hamiltonian A leads to $\epsilon_\lambda = -\hbar^2 k^2/2M + \kappa_\nu$ with κ_ν as the eigenvalue of the spinor part of A. The spatial part of ρ^{nc} can be integrated using that $\sum_{\boldsymbol{k}} \to (2\pi)^{-3} \int d\boldsymbol{k}$,

$$\rho^{nc}_{ij} = \sum_{\nu=1}^{3} \xi^{\nu}_i \xi^{\nu *}_j \frac{Li_{3/2}(e^{-\beta\kappa_\nu})}{\lambda^3_{\rm dB}}, \tag{8}$$

where $Li_{3/2}(z)$ is the polylogarithm function and $\lambda_{\rm dB} = h/\sqrt{2\pi M k_B T}$ is the thermal de Broglie wavelength. The eigendecomposition of A_{ij}, which is now a 3×3 matrix, is called the HF equation.

Before to end this section, we write here the general expressions of the GP-HF equations. We use a similar notation as in Ref. [36] but with the use of the subindices for ρ^c and ρ^{nc} as in Ref. [34]. The condensate fraction $\rho^c = N^c \boldsymbol{\Phi}\boldsymbol{\Phi}^\dagger$ is obtained by the GP equations $\delta E_{\rm HF}/\delta \phi^*_m = 0$, which are equal to

$$\begin{aligned} &\mu \boldsymbol{\Phi} = L \boldsymbol{\Phi}, \\ &L = -pF_z + qF_z^2 + c_0(N\mathbb{1}_3 + \rho^{nc}) \\ &\quad + c_1 \sum_\alpha \{{\rm Tr}[F_\alpha \rho] F_\alpha + F_\alpha \rho^{nc} F_\alpha\}, \end{aligned} \tag{9}$$

where $\alpha = x,\ y$, and z. On the other hand, the noncondensate Hamiltonian $A_{ij} = \delta E_{\rm HF}/\delta \rho^{nc}_{ji}$ has the following expression:

$$\begin{aligned} A &= L - \mu \mathbb{1}_3 - c_0 \rho^c + c_1 \sum_\alpha F_\alpha \rho^c F_\alpha \\ &= -\mu \mathbb{1}_3 - pF_z + qF_z^2 + c_0(N\mathbb{1}_3 + \rho) \\ &\quad + c_1 \sum_\alpha \{{\rm Tr}[\rho F_\alpha] F_\alpha + F_\alpha \rho F_\alpha\}. \end{aligned} \tag{10}$$

Usually, the GP-HF equations (9) and (10) are solved self-consistently [34–36]. However, we will avoid the self-consistent procedure as it is explained in the next section.

III. APPROACH AND RESULTS

We start by restricting ρ^c to a particular phase, FM, P, or AF. Each phase exhibits some symmetries in common with the full Hamiltonian (2). By a well-known result (Sec. 8.4 of Ref. [34]), the perturbation of the system ρ^{nc} inherits the common symmetries of ρ^c and $\hat{H}$, reducing its degrees of freedom. This approach simplifies the GP-HF equations from a set of equations of the components of ρ^c and ρ^{nc}, to a system of three algebraic-transcendental equations of the κ_μ energies.

Let us illustrate our approach by considering the FM phase $\boldsymbol{\Phi} = N^c(1, 0, 0)^T$. In general, one must find the variables of ρ^{nc}_{ij} and N^c, subject to the condition $N^c + N^{nc} = N$, which gives a total of nine unknown variables. However, the degrees of freedom of ρ^{nc} are reduced by its symmetries, consisting of the rotations over the z axis by a generic angle θ, $R_z(\theta) = e^{-i\theta F_z}$, inherited by the FM phase and the Hamiltonian (2) [34]. In particular, this implies that ρ^{nc} must commute with the generator F_z, and, hence, ρ^{nc} and F_z must have the same eigenvectors,

$$\rho^{nc} = \sum_{m=-1}^{1} \Lambda_m |1, m\rangle \langle 1, m|, \qquad \Lambda_m = \frac{Li_{3/2}(e^{-\beta\kappa_m})}{\lambda^3_{dB}}, \tag{11}$$

where the eigenvalues are given by Eq. (8). The atom fractions N^c and N^{nc} can be written in terms of κ_m because $N^c = N - N^{nc}$ and $N^{nc} = \sum_m \Lambda_m$, reducing the unknown variables to the three eigenenergies κ_m of the HF Hamiltonian $A = \delta E_{\rm HF}/\delta \rho^{nc}_{ji}$. Another useful visual way to infer the rotational symmetries over the quantum states, which allows to simplify the degrees of freedom, is through the stellar Majorana representation for pure [46] and mixed states [47]. The chemical potential μ is calculated by substituting the order parameter of the FM phase in the GP equations (10),

$$\mu = -p + q + c_0(\Lambda_1 + N) + c_1(N + \Lambda_1 - 2\Lambda_{-1}). \tag{12}$$

On the other hand, the eigenvalues κ_m of A are obtained after we substitute (11) in (10), yielding

$$\begin{aligned} \kappa_1^{\rm (FM)} &= (c_0 + c_1)(N - \Lambda_1 - \Lambda_0 - \Lambda_{-1}), \\ \kappa_0^{\rm (FM)} &= p - q - (c_0 + c_1)\Lambda_1 + (c_0 - c_1)\Lambda_0 + 2c_1\Lambda_{-1}, \\ \kappa_{-1}^{\rm (FM)} &= 2(p - c_1 N) - (c_0 + c_1)\Lambda_1 \\ &\quad + 2c_1\Lambda_0 + (c_0 + 5c_1)\Lambda_{-1}. \end{aligned} \tag{13}$$

Here, the superscript index denotes the spin phase of the condensate fraction ρ^c. For simplicity, we call the resulting phase, which is now a mixture of spin states as the phase of the condensate fraction ρ^c. For example, the solutions of Eqs. (13) are called the FM phase at a given temperature T and (q, p) values. We derive similar equations for the P and AF phases in Appendix B.

The maximum temperature where the HF theory predicts a spin phase $T_{\rm max}$ can be estimated by the condensation temperature of an ideal spin-1 BEC in a box $T_c^{\rm spin}$. It is known that $T_c^{\rm spin}$ is equal to the condensation temperature of an ideal scalar gas T_0 rescaled by the three internal spin-states $T_c^{\rm spin} = (1/3)^{2/3} T_0 \approx 0.48 T_0$ [36], where T_0 is calculated by the well-known formula $T_0 = 3.31\hbar^2 N^{2/3}/(k_B M)$ [2]. For our paper, we use the atomic density commonly obtained in experiments for a ^{23}Na condensate $N = 10^{14}$ cm^{-3} [11], yielding $T_0 = 1.5\ \mu$K and equal to $T_0 = 572 c_1 N/k_B$ in terms of the spin-dependent interaction. Another way to estimate $T_{\rm max}$ is by considering the fact that an atomic gas does not condensate for temperatures such that $k_B T \gg \mu$, thus, one can assume thermal energies greater than the chemical potential by an order of magnitude $k_B T \geqslant 10\mu$. For example, for the FM phase with $(q, p) = (0, 0)$, the chemical potential (12) is minimized in the hypothetic case $\Lambda_{-1} = N$ (implying $\Lambda_1 = 0$), yielding that $\mu = 26 c_1 N$ and, hence, $T_{\rm max} \approx 0.45 T_0$. A similar estimation can be calculated for the P and AF phases and for any (q, p) values. Both estimations obtained a similar $T_{\rm max}$,

and then we will study the spin-1 BEC for temperatures up to $0.4T_0$.

A. Metastable phase diagrams

The approach is applied to calculate the allowed region of each phase in the temperature interval $[0, 0.4T_0]$ and (q, p) values of up to $(\pm 3, 2)c_1N$. The results reported in this paper were obtained by solving numerically Eqs. (13), (B13), and (B21)–(B23) for the FM, P, and AF phases, respectively. Let us discuss first the HF results for $T = 0$ [48] plotted in Fig. 1, which gives the same ground-state spin-phase diagram in mean-field theory. We denote the allowed region of each phase with a primary color: the FM, P, and AF phases with blue (upper left), red (right), and yellow (lower left), respectively. Remarkably, we find also overlapping regions, implying that there could be some metastable phases upon some (q, p) values. The overlaps of the FM and P(upper-center), and the AF and P (lower-center) phases are shown with the respective secondary colors purple and orange. The boundaries of the FM, P, and AF phases are denoted with dotted, dashed, and dashed-dot lines, respectively. The solid lines delimit the region where each phase is the ground state, which minimizes the HF thermodynamic potential [34],

$$\Phi_{\rm HF} = E_{\rm HF} - TS_{\rm HF}, \tag{14}$$

with $E_{\rm HF}$ given by Eq. (6), and $S_{\rm HF}$ is the HF entropy (A4). As expected, the thermodynamic potential $\Phi_{\rm HF}$ reduces to the HF energy $E_{\rm HF}$ at $T = 0$.

The quench dynamics of a spinor condensate, i.e., its evolution after the sudden change in a control parameter, could be explained with a metastable phase diagram. For an example at hand, let us consider first that our spinor condensate is prepared in the P phase with control parameters $(q, p) = (1.5c_1N, 0)$ at $T = 0$. Here the only admissible phase is the polar one, hence, the graph of the thermodynamic potential $\Phi_{\rm HF}$ versus an order-parameter variable of ρ^c and ρ^{nc}, included in the set $\Gamma = \{\phi_m, \rho^{nc}_{ij}\}$, has a global minimum. We plot a sketch of $\Phi_{\rm HF}$ versus a variable of the set Γ in Fig. 1. Essentially, there are three possible $\Phi_{\rm HF}$s with substantial changes to affect the quench dynamics of the spinor condensate. We exemplify each case in Fig. 1, corresponding to the points with $p = 0$ and the following values of q:

(1) $q = 0.5c_1N$: $\Phi_{\rm HF}$ has now two minima related to the P and AF phases. The atoms of the spinor condensate would rather stay in the P phase by the difference $\Delta\Phi_{\rm HF}$.

(2) $q = -0.5c_1N$: Here, we also have two admissible phases, but now the AF phase is the ground state. The quantum tunneling is now stimulated to the AF phase. The smaller is $\Delta\Phi_{\rm HF}$ between the phases, more atoms oscillate between the phases with respect to the time. However, dissipation-energy effects would favor the tendency of the atoms to stay in the ground state.

(3) $q = -1.5c_1N$: The AF phase is now the only admissible phase, producing an abrupt change of the atoms without oscillations between the phases.

In particular, Ref. [29] reported the experimental observation of three different types of quench dynamics given by the sudden change in q and with fixed magnetization of the spinor condensate. The three types of quench dynamics fit qualitatively well with the ones explained above. The metastable phase diagram in Fig. 1 also helps us to predict similar quench processes given by a sudden change in the p parameter instead of q or by a more general sudden change involving the (q, p) values.

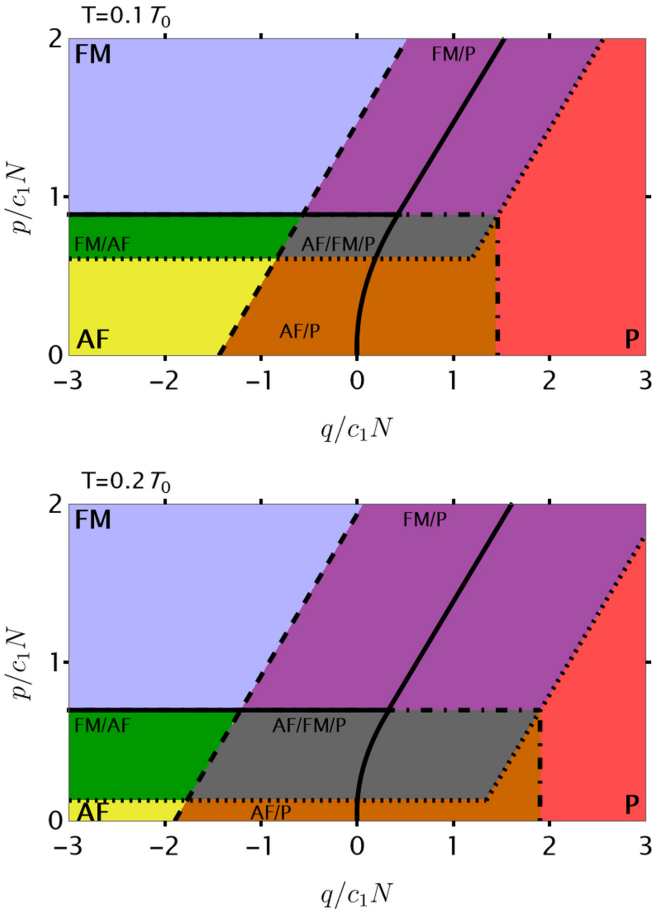

FIG. 2. Metastable phase diagrams at temperatures T equal to $0.1T_0$ (top) and $0.2T_0$ (bottom). The conventions of the colors, lines, and labels are as in Fig. 1. There are two new overlapping regions, the green FM and AF (middle-left) zone and the dark-gray AF, FM, and P area (center) where the three phases coexist.

We will discuss now the results obtained at finite temperatures. We plot in Fig. 2 the metastable phase diagram for $T/T_0 = 0.1$ and 0.2, which includes two new regions: the green region (middle-left) associated with the overlapping of the FM and AF phases, and a dark-gray region (center) where the three phases coexist. The last one is associated with a free-energy $\Phi_{\rm HF}$ with three critical points, a new scenery not seen at $T = 0$. The overlapping regions among the phases are also affected by the temperature, implying that the same quench processes described above can be produced by a change in T instead of q. For instance, let us consider a BEC in the FM phase at $T = 0.2T_0$ over the parameters $(q, p) = (-2, 0.9)c_1N$. If one cools down the BEC to nearly 0 K, the FM phase is no longer an allowed phase, and the atoms would migrate to the AF phase, the only available phase at this (q, p) point.

The approach applied in this paper not only leads to obtain the whole region of each phase, but also to the physical nature

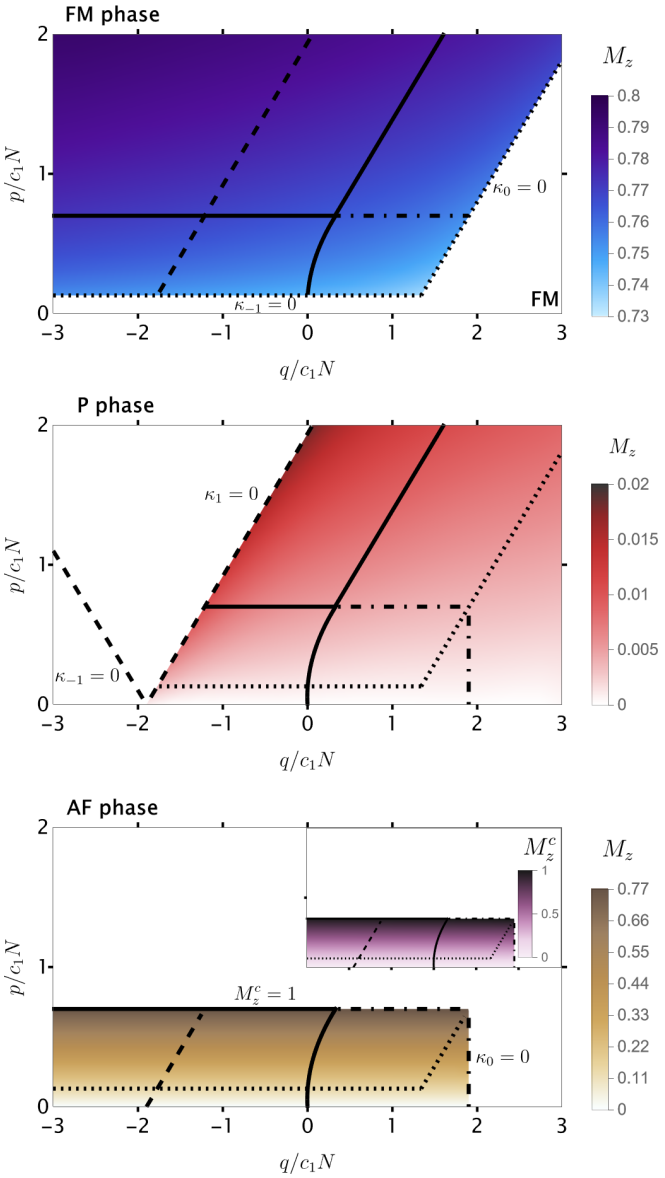

FIG. 3. Magnetization per atom over the z axis M_z of the FM, P, and AF phases at $T = 0.2T_0$, respectively. The boundaries of each region are specified as in Fig. 1. The inset graphic in the AF phase is the magnetization per atom of the condensate fraction M_z^c. The color (grayscale) legend applies only for the admissible region of each phase.

of their boundaries. The HF approximation inserts the new ingredient of the thermal atoms ρ^{nc}, populated with respect to the energies κ_ν plus the kinetic energy. For the atoms in the thermal cloud with $\boldsymbol{k} \approx 0$, the energy levels are given only by κ_ν, which are interpreted as the additional energy to add an atom in the thermal cloud ρ^{nc} instead of ρ^c. Therefore, $\kappa_\nu > 0$ for all $\nu = 1$–3, otherwise it is energetically favorable or equal to populate ρ^{nc} than ρ^c. A phase would be forbidden as long $\kappa_\nu \leqslant 0$ for any ν. We list here the physical conditions of the emergence of the boundaries of each phase seen in Figs. 1 and 2 (see also Fig. 3):

(1) FM phase boundary (dotted lines): ρ^{nc} and F_z share the same eigenstates $|1, m\rangle$, with $m = 0, \pm 1$. The two boundaries are given when κ_0 or $\kappa_{-1} = 0$ where the subindex denotes the quantum number m.

(2) P phase boundary (dashed lines): The eigenvectors of ρ^{nc} are, again, the states $|1, m\rangle$, and the boundary is given by the condition $\kappa_1 = 0$. The condition $\kappa_{-1} = 0$ is also plotted in Fig. 3.

(3) AF phase boundary (dashed-dot lines): One of the eigenvectors of ρ^{nc} is equal to state $|1, 0\rangle$, and the other two are quantum superpositions of states $|1, \pm 1\rangle$ [36] (see also Appendix B). The vertical bound of the AF phase is given by $\kappa_0 = 0$, and the horizontal bound is a generalization of (5), $M_z^c \equiv \mathrm{Tr}(\rho^c F_z)/N^c = 1$.

The system of three equations of the κ_ν energies for each phase leads us to analytic approximations of the bounds in terms of the (q, p, T) variables for $T < T_0$ (Appendix B),

$$\begin{aligned} &(\mathrm{FM})\kappa_0 = p - q + F_0(T), \quad \kappa_{-1} = 2(p - c_1N) + F_{-1}(T), \\ &(\mathrm{P}) \quad \kappa_{\pm 1} = q \mp p + c_1N + G_{\pm 1}(T), \\ &(\mathrm{AF})\kappa_0 = c_1N - q + H_0(T), \quad p = c_1N + H'(T), \end{aligned} \tag{15}$$

where the last equation is given by the condition $M_z^c = 1$. The functions F_ν, G_ν, H_0, and H' depend only on the temperature, and all go identically to zero when $T = 0$ (Appendix B). The approximations are valid up to $O(k_1^2)$ with $k_1 = c_1N/k_BT_0$, and they agree well with the numerical results obtained in the interval of $T \in [0, 0.2T_0]$. The equations of the boundaries of each phase are deduced in Appendix B. One can observe that Eqs. (15) are linear with respect to the parameters p and q. Hence, the analytic approximation of the bounds are straight lines on the (q, p) space such that its slope remains invariant but its position depends on T for $T < T_0$. The regions of the phases increase along all the boundaries as we increase the temperature (see Appendix B) except along the horizontal bound of the AF phase.

B. Physical properties

The BEC phases can be distinguished among each other by their physical properties. In Fig. 3, we plot the magnetization per atom $M_z \equiv \mathrm{Tr}(\rho F_z)/N$ of each phase in its allowed region at $T = 0.2T_0$. The color density of each plot is normalized differently, and we denote the boundaries as we did in Fig. 1. The most of the magnetization of each phase arises from the condensate fraction ρ^c, whereas the small deviations can be understood by the physical origin of the boundaries:

(1) FM phase: Its magnetization M_z decreases in the (q, p) values close to the boundaries. This is true because as κ_m decreases, more atoms are populated to state $|1, m\rangle$, which it has zero or negative magnetization for $m = 0, -1$, respectively.

(2) P phase: The magnetization increases for the (q, p) values adjacent to the line $\kappa_1 = 0$ and also further away from the $\kappa_{-1} = 0$ condition. The BEC has null magnetization in the line $p = 0$ because it is equidistant to both conditions $\kappa_{\pm 1} = 0$ (15).

(3) AF phase: Similar as for the $T = 0$ case, the maximum value of p for the AF phase is when $M_z^c = 1$, i.e.when the AF phase is identical to the FM phase. M_z decreases as p decreases with minimum $M_z = 0$ for $p = 0$. Also, the numerical calculations reveal that M_z is independent of the q parameter, which is also confirmed with the analytic approximations for

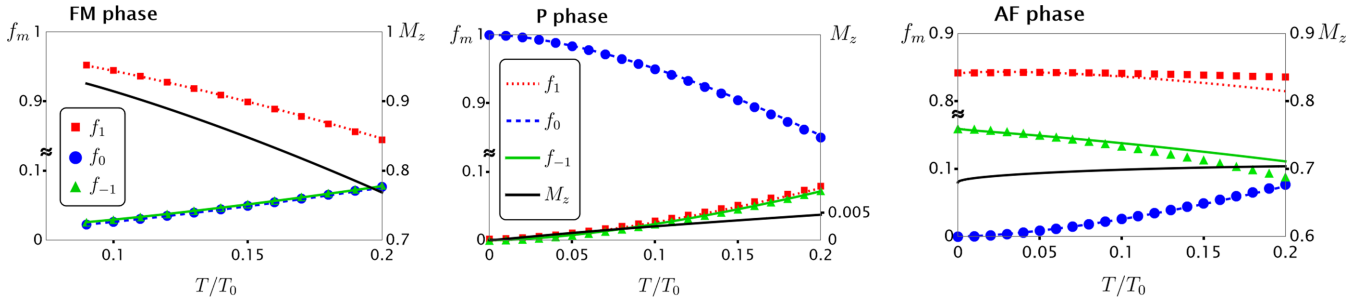

FIG. 4. The fractions $f_m = \langle 1, m|\,\rho\,|1, m\rangle\,/N$ as functions of the temperature for the FM, P, and AF phases calculated numerically in the triple point at $T = 0.2T_0$, $(q, p) = (0.32, 0.68)c_1N$. The lines correspond to the fractions using the analytic expressions of κ_ν (Appendix B), which agrees well with the numerical results denoted by the squares (red), circles (blue), and triangles (green), respectively. The black solid line corresponds to M_z with the scale denoted on the right axis.

$T < T_0$ (Appendix C). The inset plot of the AF phase shows the condensate magnetization M_z^c. By comparing both figures, one can deduce that the noncondensate fraction ρ^{nc} would play against the magnetization of the condensation fraction as discussed in Ref. [36].

Another way to distinguish the phases is by their population fractions of the $|1, m\rangle$ states, which can be monitored experimentally by absorption images [12,49]. In Fig. 4, we plot the fractions $f_m \equiv \langle 1, m|\,\rho\,|1, m\rangle\,/N$ versus the temperature for the (q, p) values of the triple-point at $T = 0.2T_0$, $(0.32, 0.68)c_1N$. The P and AF phases exist for the temperatures $T \in [0, 0.2T_0]$. On the other hand, the FM phase only exists at the temperature interval $T/T_0 \in [0.09, 0.2]$. For the FM and P phases, their respective fractions begin to decrease as one increases the temperature, whereas the other two projections are populated equally in the thermal cloud. The AF phase increases (decreases) the fraction f_0 ($f_{\pm1}$) as one increases the temperature. The change in f_1 from $T = 0$ to $T = 0.2T_0$ is more notorious as one reduces the p parameter (Appendix D). This result provide us a way to distinguish the AF and FM phases by comparing the evolution of the f_1 fraction with respect to the temperature. Note that the change f_1 from $T = 0$ to $T = 0.2T_0$ is, at least, one order of magnitude greater for the FM phase as for the AF phase (see Fig. 4 and Appendix C). The black lines of Fig. 4 correspond to $M_z = f_1 - f_{-1}$. The magnetization of FM phase is screened by the thermal atoms. On the other side, the magnetic sublevels $m = 1$ ($m = 0$) in ρ^{nc} are more populated than the other magnetic sublevels in the P (AF) phase. Consequently, M_z increases with respect to the temperature.

C. Phase-transition boundaries

To end this section, we plot the phase diagrams for different temperatures in Fig. 5 where the ground states minimize the thermodynamic potential $\Phi_{\rm HF}$. The FM phase reaches lower p values as the temperature is increased as mentioned in Ref. [36]. Another feature we reveal here is that the FM phase also increases to the positive interval of the q parameter. This can be better understood as we compare the thermodynamic potentials of the FM and P phases using the analytic expression of the energies κ_ν (Appendix B), which leads to

$$\Phi_{\rm HF}^{\rm (FM)} - \Phi_{\rm HF}^{\rm (P)} = \frac{Ng}{2}[2(q-p) + c_1Ng] + O\left(k_1^2\right), \qquad (16)$$

where $g = g(T) = 1 - 3\zeta(3/2)/\lambda_{\rm dB}^3 N$ with $\zeta(z)$ as the Riemann ζ function. The previous equation predicts the linear behavior of the FM-P boundary in the (q, p) parameters. The intersection between the AF-FM and FM-P boundaries is the triple-point of the phase diagram, and its position decreases on the p and q parameters as the temperature T is increased (see Fig. 5).

IV. CONCLUSIONS

We have shown that a minimal many-body HF theory that fully accounts for the Hamiltonian and order parameter symmetries of a spin-1 antiferromagnetic BEC allows us to describe the presence of regions where metastable phases could arise at zero and finite temperatures. The metastable spin-phase diagram provides a useful and complementary way to understand the different types of quench dynamics observed in experiments [29] among other phenomena. In addition, the metastable spin phases can be created experimentally by the stimulation of a state transition via rf resonances [22–24] or the quench process [28] as we discussed in our paper. After that, the spin phases can be easily distinguished in the laboratory by their physical properties, e.g., its magnetization or with a time-of-flight imaging technique followed by a Stern-

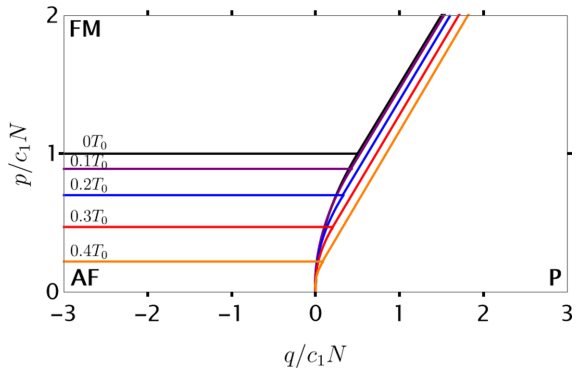

FIG. 5. Temperature dependence of the phase diagram (solid line) for $T/T_0 = 0, 0.1, \ldots, 0.4$. The FM-AF boundary as a function of the temperature was described in Ref. [36]. The behavior of the FM-P boundary is explained by the difference among the HF potentials of the phases (16).

Gerlach spin separation to determine the atom fractions of each magnetic level [21–24,28]. In particular, we enlightened two unique properties of the AF phase: Its magnetization is independent of the quadratic Zeeman coefficient q, and the atom fraction f_1 of the condensate remains basically invariant for sufficiently high values of p as the temperature is increased. Finally, we found a significant shift of the FM-P boundary with temperature and derived an analytical expression for its behavior valid at low temperatures.

This paper opens up a number of routes that can be explored within the framework presented here for the study of spin-1 antiferromagnetic BEC. Indeed, the approach is quite general as it can be straightforwardly applied to spinor condensates with different spin-dependent interactions and/or higher internal spin values. We should remark that whereas the ground-state configuration of any spinor condensate is understood to be stable by definition, the emergent metastable states could be unstable under some weak perturbations or instabilities. Even tough, the approach is still suitable, and it can be formally extended, e.g., through the aid of the Hessian of the thermodynamic potential to characterize the instabilities of the metastable phases.

ACKNOWLEDGMENTS

E.S.-E. would like to acknowledge support from the postdoctoral fellowships of CONACyT and DGAPA-UNAM. F.M. acknowledges support from DGAPA-UNAM through the Project PAPIIT No. IN113920.

APPENDIX A: EXPRESSIONS OF E_s AND $S_{\rm HF}$

Here we derive the spatial energy E_s in Eq. (6) and the spatial entropy S_{HF} of the Hartree-Fock theory, which can be written in terms of the κ_ν eigenenergies,

$$\rho_{ij}^{nc} = \sum_{\boldsymbol{k},\nu} n_\lambda \xi_i^\nu e^{i\boldsymbol{k}\cdot\boldsymbol{r}} \left(\xi_j^\nu e^{i\boldsymbol{k}\cdot\boldsymbol{r}}\right)^* = \sum_\nu \xi_i^\nu \xi_j^{\nu *} (2\pi)^{-3}(4\pi)\int_0^\infty k^2 (z_\nu^{-1} e^{(\beta\hbar^2k^2)/2M} - 1)^{-1} dk, \tag{A1}$$

where $z_\nu = e^{-\beta\kappa_\nu}$. By a change of variable $x = \beta\hbar^2k^2/2M$, we deduce that Eq. (8),

$$\rho_{ij}^{nc} = \sum_\nu \xi_i^\nu \xi_j^{\nu *} \frac{4\pi\sqrt{2}(Mk_BT)^{3/2}}{h^3}\int_0^\infty x^{1/2}(z_\nu^{-1}e^x - 1)^{-1}dx = \sum_\nu \xi_i^\nu \xi_j^{\nu *} \frac{Li_{3/2}(z_\nu)}{\lambda_{\rm dB}^3}, \tag{A2}$$

with $\lambda_{\rm dB} = h/(2\pi M k_B T)^{1/2}$ as the thermal de Broglie wavelength and $Li_j(z)$ as the polylogarithm function. Analogously, the spatial energy E_s is equal to

$$E_s = \frac{\hbar^2}{2M}\sum_{\boldsymbol{k},\nu,i} \xi_i^\nu e^{i\boldsymbol{k}\cdot\boldsymbol{r}} \left(\xi_i^\nu e^{i\boldsymbol{k}\cdot\boldsymbol{r}}\right)^* n_\lambda k^2 = \sum_\nu \frac{3Li_{5/2}(z_\nu)}{2\beta\lambda_{\rm dB}^3}. \tag{A3}$$

Finally, we use the same limit of the wave number for the HF entropy [34],

$$S_{\rm HF} = -k_B\sum_\lambda n_\lambda \ln n_\lambda - (1+n_\lambda)\ln(1+n_\lambda) = \frac{k_B}{\lambda_{\rm dB}^3}\sum_\nu \frac{5}{2}Li_{5/2}(z_\nu) - Li_{3/2}(z_\nu)\ln z_\nu. \tag{A4}$$

APPENDIX B: EQUATIONS FOR THE κ_ν ENERGIES AND THEIR ANALYTIC APPROXIMATIONS

To simplify the equations and calculations, we scale the following variables:

$$\begin{pmatrix}\bar{p}\\ \bar{q}\\ \bar{L}\\ \bar{\mu}\\ \bar{A}\\ \bar{\kappa}_\nu\end{pmatrix} = \begin{pmatrix}p\\ q\\ L\\ \mu\\ A\\ \kappa_\nu\end{pmatrix}\Big/|c_1|N, \qquad \begin{pmatrix}\bar{N}^c\\ \bar{N}^{nc}\\ \bar{\rho}^c\\ \bar{\rho}^{nc}\\ \bar{\rho}\end{pmatrix} = \begin{pmatrix}N^c\\ N^{nc}\\ \rho^c\\ \rho^{nc}\\ \rho\end{pmatrix}\Big/N, \tag{B1}$$

$$\bar{c}_0 = \frac{c_0}{|c_1|}, \qquad \bar{T} = \frac{T}{T_0}.$$

The condensate and noncondensate fractions satisfy that $\bar{N}^c + \bar{N}^{nc} = 1$. $\bar{\rho}^{nc}$ is written as

$$\bar{\rho}_{ij}^{nc} = \sum_\nu \Lambda_\nu \xi_i^\nu \xi_j^{\nu *}, \qquad \Lambda_\nu = \frac{Li_{3/2}(e^{-z_\nu})}{N\lambda_{\rm dB}^3}, \tag{B2}$$

with $\bar{N}^{nc} = \sum_\nu \Lambda_\nu$ and

$$z_\nu = \left(\frac{c_1 N}{k_B T_0}\right)\left(\frac{\bar{\kappa}_\nu}{\bar{T}}\right) = k_1\frac{\bar{\kappa}_\nu}{\bar{T}}. \tag{B3}$$

In the following, we will work with the scaled variables, and we will suppress the bar symbol in each term. We also define $\eta = c_1/|c_1|$ to express our results for any type of interaction: ferromagnetic ($\eta = -1$), antiferromagnetic ($\eta = 1$), or without spin-dependent interactions ($\eta = 0$). Equations (9) and (10) are reduced to

$$\mu\boldsymbol{\Phi} = L\boldsymbol{\Phi}, \qquad L = -pF_z + qF_z^2 + c_0(\mathbb{1}_3 + \rho^{nc}) + \eta\sum_\alpha \{{\rm Tr}[F_\alpha\rho]F_\alpha + F_\alpha\rho^{nc}F_\alpha\}, \tag{B4}$$

$$A = -\mu\mathbb{1}_3 - pF_z + qF_z^2 + c_0(\mathbb{1}_3 + \rho) + \eta\sum_\alpha \{{\rm Tr}[\rho F_\alpha]F_\alpha + F_\alpha\rho F_\alpha\}. \tag{B5}$$

Now, we will deduce the system of equations for κ_ν of each phase. The numerical results exposed through this paper were obtained by solving Eqs. (B7), (B13), and (B21)–(B23) for the FM, P, and AF phases, respectively. We also derive the analytic approximations for κ_ν for each phase. The analytical approximations agree well with the numerical results in the low-temperature regime (see Fig. 4).

1. FM phase

The ferromagnetic phase was already discussed in Sec. III where the chemical potential and the eigenenergies $\kappa_m^{(\mathrm{FM})}$ (12) and (13) in the scaled variables are given by

$$\mu = -p + q + c_0(\Lambda_1 + 1) + \eta(1 + \Lambda_1 - 2\Lambda_{-1}), \tag{B6}$$

$$\begin{aligned}\kappa_1^{(\mathrm{FM})} &= (c_0 + \eta)(1 - \Lambda_1 - \Lambda_0 - \Lambda_{-1}),\\ \kappa_0^{(\mathrm{FM})} &= p - q - (c_0 + \eta)\Lambda_1 + (c_0 - \eta)\Lambda_0 + 2\eta\Lambda_{-1},\\ \kappa_{-1}^{(\mathrm{FM})} &= 2(p - \eta) - (c_0 + \eta)\Lambda_1 + 2\eta\Lambda_0 + (c_0 + 5\eta)\Lambda_{-1}.\end{aligned} \tag{B7}$$

Here, the superscript index denotes the spin phase. Once we write the right-hand side of the equations as functions of the energies $\kappa_\nu^{(\mathrm{FM})} = K_\nu^{(\mathrm{FM})}(\kappa_1^{(\mathrm{FM})}, \kappa_0^{(\mathrm{FM})}, \kappa_1^{(\mathrm{FM})})$, the resulting algebraic-transcendental equations cannot be solved analytically. However, we can obtain useful analytic expressions through some approximations. The first approximation is given by

$$\begin{aligned}\Lambda_\nu &= \frac{Li_{3/2}(e^{-z_\nu})}{N\lambda_{\mathrm{dB}}^3}\\ &\approx \frac{1}{N\lambda_{\mathrm{dB}}^3}\left[\zeta\left(\frac{3}{2}\right) - 2\sqrt{\pi z_\nu} - \zeta\left(\frac{1}{2}\right)z_\nu + O\left(z_\nu^2\right)\right],\\ z_\nu &= \frac{k_1\kappa_\nu}{T},\end{aligned} \tag{B8}$$

which is valid for our case because we are interested in the qualitative behavior around $k_1\kappa_\mu/T \approx 0$ where $k_1 = c_1 N/k_B T_0 = 1.75(10^{-3})$. Here $\zeta(z)$ is the Riemann ζ function. We expand the analytic approximations with respect to k_1 to expose compact expressions. In addition, the numerical results tell us that $\kappa_1 > \kappa_0, \kappa_{-1}$. Then, we can also assume on the right-hand side of (B7) that

$$\kappa_\nu^{(\mathrm{FM})} \approx K_\nu^{(\mathrm{FM})}\left(\kappa_1^{(\mathrm{FM})}, 0, 0\right). \tag{B9}$$

Thus, Eqs. (B7) can now be solved analytically leading to

$$\begin{aligned}\kappa_1^{(\mathrm{FM})} &= g(c_0 + \eta) - 2k_2T[\pi g k_1(c_0 + \eta)^3]^{1/2}\\ &\quad + k_1k_2T^{1/2}(c_0 + \eta)^2\left[g\zeta\left(\frac{1}{2}\right) + 2\pi k_2T^{3/2}\right] + O(k_1^2),\\ \kappa_0^{(\mathrm{FM})} &= p - q + 2k_2T[\pi g k_1(c_0 + \eta)^3]^{1/2} + k_1k_2T^{1/2}(c_0 + \eta)^2\\ &\quad \times\left[g\zeta\left(\frac{1}{2}\right) - 2\pi k_2T^{3/2}\right] + O\left(k_1^2\right),\\ \kappa_{-1}^{(\mathrm{FM})} &= 2(p - \eta g) + 2k_2T[\pi g k_1(c_0 + \eta)^{3/2}]^{1/2}\\ &\quad + k_1k_2T^{1/2}(c_0 + \eta)^2\left[g\zeta\left(\frac{1}{2}\right) - 2\pi k_2T^{3/2}\right] + O\left(k_1^2\right),\end{aligned} \tag{B10}$$

where we have defined

$$g = g(T) = 1 - \frac{3}{\lambda_{\mathrm{dB}}^3 N}\zeta\left(\frac{3}{2}\right) = 1 - 3k_2T^{3/2}\zeta\left(\frac{3}{2}\right), \tag{B11}$$

in which $k_2 = 1/\lambda_0^3 N$ where λ_0 is the de Broglie wavelength at $T = T_0$. The functions $F_\nu(T)$ in (15) are given by the difference between Eqs. (B10) and their evaluation at $T = 0$, $F_\nu(T) = \kappa_\nu^{(\mathrm{FM})} - \kappa_\nu^{(\mathrm{FM})}|_{T=0}$.

2. P phase

The polar phase $\mathbf{\Phi} = (0, 1, 0)^T$ is solved similarly as the FM phase. In this case, the GP equations lead to

$$\mu = c_0(1 + \Lambda_0) + \eta(\Lambda_1 + \Lambda_{-1}). \tag{B12}$$

The eigenvectors of A and ρ^{nc} are, again, states $|1, m\rangle$. The exact equations of κ_ν are given by

$$\begin{aligned}\kappa_1^{(\mathrm{P})} &= q - p + \eta + c_0\Lambda_1 - c_0\Lambda_0 - 3\eta\Lambda_{-1},\\ \kappa_0^{(\mathrm{P})} &= c_0(1 - \Lambda_1 - \Lambda_0 - \Lambda_{-1}),\\ \kappa_{-1}^{(\mathrm{P})} &= q + p + \eta - 3\eta\Lambda_1 - c_0\Lambda_0 + c_0\Lambda_{-1}.\end{aligned} \tag{B13}$$

Here $\kappa_0 > \kappa_{\pm1}$ in the low-temperature regime. Then, one can assume

$$\kappa_\nu^{(\mathrm{P})} \approx K_\nu^{(\mathrm{P})}\left(0, \kappa_0^{(\mathrm{P})}, 0\right), \tag{B14}$$

which gives the following approximations:

$$\begin{aligned}\kappa_{\pm1}^{(\mathrm{P})} &= \mp p + q + \eta g + 2k_2T\left(k_1\pi c_0^3 g\right)^{1/2}]\\ &\quad + k_1k_2c_0^2T^{1/2}\left[\zeta\left(\frac{1}{2}\right)g + 2\pi k_2T^{3/2}\right] + O\left(k_1^2\right),\\ \kappa_0^{(\mathrm{P})} &= c_0 g + 2k_2T\left(k_1\pi c_0^3 g\right)^{1/2} + k_1k_2c_0^2T^{1/2}\\ &\quad \times\left[\zeta\left(\frac{1}{2}\right)g + 2\pi k_2T^{3/2}\right] + O\left(k_1^2\right).\end{aligned} \tag{B15}$$

Here, we observe that the energies $\kappa_{\pm1}^{(\mathrm{P})}$ only differ by the sign of p. The functions $G_\nu(T)$ of (15) are obtained similarly as $F_\nu(T)$ for the FM phase $G_\nu(T) = \kappa_\nu^{(\mathrm{P})} - \kappa_\nu^{(\mathrm{P})}|_{T=0}$.

3. AF phase

The family of states of the AF phase are given by the order parameter $\mathbf{\Phi} = (\phi_1, \phi_0, \phi_{-1}) = (\cos\chi, 0, \sin\chi)^T$ with $\chi \in (0, \pi/4]$. For a general χ, ρ^c is symmetric under a rotation by π about the z axis $R_z(\pi)$ and by the conjugation operator C, which is equivalent to a reflection over the yz plane. Both operators are also symmetries of the Hamiltonian $\hat{H}$ (2). Hence, ρ^{nc} must possess the same symmetries, implying that

$$\rho^{nc} = \begin{pmatrix} a & 0 & D\\ 0 & b & 0\\ D & 0 & c\end{pmatrix}, \tag{B16}$$

where D must be real. State $|1, 0\rangle$ would be an eigenvector of ρ^{nc} and $b = \Lambda_0$. For the other two eigenvectors, we follow a similar analysis of Eqs. (B5) as in Ref. [36]. Also, we only consider antiferromagnetic interactions $\eta = 1$. The GP equations for the ρ^c and ρ^{nc} mentioned above imply that [36]

$$\begin{pmatrix} -\tilde{p} - \tilde{\mu} & C_-D\\ C_-D & \tilde{p} - \tilde{\mu}\end{pmatrix}\begin{pmatrix}\phi_1\\ \phi_{-1}\end{pmatrix} = \begin{pmatrix}0\\ 0\end{pmatrix}, \tag{B17}$$

where

$$\tilde{p} = p - N^c\cos(2\chi) - \frac{(c_0+3)(a-c)}{2},$$
$$\tilde{\mu} = \mu - \left(q + c_0 + b + \frac{C_+(a+c)}{2}\right),$$
$$C_\pm = c_0 \pm 1. \tag{B18}$$

Let us remember that $N^c = 1 - N^{nc} = 1 - (a+b+c)$. The eigensystem (B17) yields [36]

$$\tilde{\mu} = \pm\sqrt{\tilde{p}^2 + C_-^2 D^2}, \tag{B19}$$

$$\tan(\chi) = -\frac{C_- D}{\tilde{p} + \sqrt{\tilde{p}^2 + C_-^2 D^2}}, \tag{B20}$$

where we assume the negative value of $\tilde{\mu}$ to consider the lowest chemical potential. Equation (B20) implies that D is negative because $\chi \in [0, \pi/4]$. On the other hand, the Hamiltonian A has, as we expected, state $|1,0\rangle$ as an eigenvector with

$$\kappa_0 = c_0(1+\Lambda_0) + 1 - \Lambda_0 - \mu. \tag{B21}$$

The other two eigenvectors are deduced by the reduced 2×2 Hamiltonian $\tilde{A}$ that involves only the components $|1,\pm 1\rangle$,

$$\tilde{A} = \left(-\tilde{\mu} + \frac{C_+ N^c}{2}\right)\mathbb{1}_2 + \begin{pmatrix} -\tilde{p} + \frac{C_+}{2}N^c\cos(2\chi) & C_-(N^c\cos\ \chi\ \sin\ \chi + D) \\ C_-(N^c\cos\ \chi\ \sin\ \chi + D) & \tilde{p} - \frac{C_+}{2}N^c\cos(2\chi) \end{pmatrix}.$$

The eigenvalues of $\tilde{A}$ are equal to [36]

$$\kappa_\pm = -\tilde{\mu} + \frac{C_+}{2}N^c \pm \sqrt{\left(\tilde{p} - \frac{C_+ N^c\cos(2\chi)}{2}\right)^2 + C_-^2(N^c\cos\ \chi\ \sin\ \chi + D)^2}. \tag{B22}$$

The $\kappa_\pm$ energies would give the expression of the eigenvalues of ρ^{nc}, which implies that

$$\frac{a+c}{2} \mp \sqrt{\left(\frac{a-c}{2}\right)^2 + D^2} = \Lambda_\pm\,. \tag{B23}$$

The Hamiltonian $\tilde{A}$ and ρ^{nc} have common eigenvectors, concluding that [36]

$$C_-(D + N^c\sin\ \chi\ \cos\ \chi)\frac{a-c}{2} = \left(\frac{C_+}{2}N^c\cos(2\chi) - \tilde{p}\right)D. \tag{B24}$$

For the FM and P phases, the unknowns quantities were given by the energies κ_ν, and we only needed three equations (B7) and (B13), respectively. In this case, we have five unknown quantities (χ, D, κ_ν) to determine with Eqs. (B20), (B21), (B23), and (B24). The variables χ and D can be written in terms of the a, b, c variables (and then with κ_ν) with Eqs. (B20) and (B24). In particular, the equation for χ is given by

$$\cos^2\chi = \frac{2(c_0+3)N^c + \sqrt{4[1-c_0(c_0+4)]p(a-c) + 8[c_0(c_0+2)-1](a-c)^2 + (c_0+1)^2p^2} - 4(c_0+2)(a-c) + (c_0+5)p}{4(c_0+3)N^c}. \tag{B25}$$

The resulting equations for χ and D can be substituted in Eqs. (B21) and (B23) to obtain the system of three equations for the energies κ_ν. We solve the final equations numerically to obtain the main results of the text.

Now, let us calculate the analytic approximations for κ_ν closer to the bounds,

$$\kappa_0^{(\mathrm{AF})} = 0,$$
$$M_z^c = 1 \Longleftrightarrow \chi = 0. \tag{B26}$$

First, we remark from (B20) that $\chi = 0$ implies that $D = 0$. Hence, we consider that $\chi \approx 0$, $D \approx 0$ and $\kappa_0 \approx 0$ in (B22) and (B23) that yields

$$a \approx \Lambda_+ \approx k_2 T^{3/2}\left[\zeta\left(\frac{3}{2}\right) - 2\sqrt{\frac{\pi k_1\kappa_+}{T}} - \zeta\left(\frac{1}{2}\right)\frac{k_1\kappa_+}{T}\right],$$

$$c \approx \Lambda_- \approx k_2 T^{3/2}\left[\zeta\left(\frac{3}{2}\right) - 2\sqrt{\frac{\pi k_1\kappa_-}{T}} - \zeta\left(\frac{1}{2}\right)\frac{k_1\kappa_-}{T}\right],$$

$$b = \Lambda_0 \approx \Lambda_0(\kappa_0 = 0) = k_2 T^{3/2}\zeta\left(\frac{3}{2}\right). \tag{B27}$$

with

$$\kappa_+ \approx (c_0+1)N^c \approx (c_0+1)\left[a - c - k_2 T^{3/2}\zeta\left(\frac{3}{2}\right)\right],$$
$$\kappa_- \approx 2\left[p - N^c - (c_0+3)\left(\frac{a-c}{2}\right)\right]$$
$$\approx 2\left[p - 1 + a + c + k_2 T^{3/2}\zeta\left(\frac{3}{2}\right)\right] - (c_0+3)(a-c). \tag{B28}$$

We linearize Eqs. (B27) with respect to a and c, and we solve them. The expressions up to first order with respect to k_1 are

$$a = \frac{k_2 T^{3/2}\zeta\left(\frac{3}{2}\right)}{2} - \frac{(c_0+1)k_1k_2T^{1/2}}{2\zeta\left(\frac{3}{2}\right)}\left\{\zeta\left(\frac{1}{2}\right)\zeta\left(\frac{3}{2}\right)g + 4\pi g'\right\} + O\left(k_1^2\right),$$
$$c = \frac{k_2 T^{3/2}\zeta\left(\frac{3}{2}\right)}{2} + \frac{k_1k_2T^{1/2}}{\zeta\left(\frac{3}{2}\right)}\left\{\zeta\left(\frac{1}{2}\right)\zeta\left(\frac{3}{2}\right)(g-p) + 4\pi(g'-p)\right\} + O\left(k_1^2\right), \tag{B29}$$
$$b = \Lambda_0 \approx \Lambda_0(\kappa_0 = 0) = k_2 T^{3/2}\zeta\left(\frac{3}{2}\right).$$

with $g' = 1 - 2k_2T^{3/2}\zeta(3/2)$. The horizontal bound $\cos\chi = 1$ in Eq. (B25) gives a quadratic equation for p. The solution that coincides with $p = 1$ at $T = 0$ is, by substituting (B29), equal to

$$p = g' - \frac{k_1k_2T^{1/2}}{(c_0+1)\zeta\left(\frac{3}{2}\right)}\left\{c_0(c_0+1)\left[4\pi g' + \zeta\left(\frac{1}{2}\right)\zeta\left(\frac{3}{2}\right)\right]\right.$$
$$\left. - (c_0+2)(3c_0+1)k_2T^{3/2}\zeta\left(\frac{1}{2}\right)\zeta\left(\frac{3}{2}\right)^2\right\} + O\left(k_1^2\right). \tag{B30}$$

The expression of $H'(T)$ in Eq. (15) is given by the difference between the right-hand side of Eq. (B30) and its evaluation at $T = 0$.

Finally, let us approximate the vertical bound $\kappa_0^{(\mathrm{AF})} = 0$. We use Eq. (B21) with $\tilde{\mu} \approx -\tilde{p}$,

$$\kappa_0 \approx (c_0-2)\Lambda_0 + 1 + \tilde{p} - q - (c_0+1)\frac{(a+c)}{2}$$
$$= (c_0-2)\Lambda_0 + 1 + p - N^c\cos(2\chi) - \frac{(c_0+3)(a-c)}{2}$$
$$-q - (c_0+1)\frac{(a+c)}{2}. \tag{B31}$$

We approximate Λ_0 on the right-hand side of the equation with (B8), and we solve the resulting equation for κ_0,

$$\kappa_0^{(\mathrm{AF})} = 1 - q + \frac{c_0-5}{2}k_2T^{3/2}\zeta\left(\frac{3}{2}\right) + \frac{k_1k_2T^{1/2}}{(c_0+1)\zeta\left(\frac{3}{2}\right)}$$
$$\times\left\{(k_3g + 4c_0p)\zeta\left(\frac{1}{2}\right)\zeta\left(\frac{3}{2}\right) + 4\pi(k_3g' + 4c_0p)\right\}$$
$$+ O\left(k_1^2\right). \tag{B32}$$

with $k_3 = (c_0-1)(c_0^2+2c_0-1)$. We can observe that the condition $\kappa_0^{(\mathrm{AF})} = 0$ also depends on p and then the boundary line is not a vertical line. However, $k_3 \gg 4c_0p$ for the values that we consider in this paper for p and T. Hence, one can neglect the term $4c_0p$,

$$\kappa_0^{(\mathrm{AF})} \approx 1 - q + \frac{c_0-5}{2}k_2T^{3/2}\zeta\left(\frac{3}{2}\right) + \frac{k_1k_2k_3T^{1/2}}{(c_0+1)\zeta\left(\frac{3}{2}\right)}$$
$$\times\left\{g\zeta\left(\frac{1}{2}\right)\zeta\left(\frac{3}{2}\right) + 4\pi g'\right\} + O\left(k_1^2\right). \tag{B33}$$

From the previous equation, one can obtain the expression of $H_0(T)$ of (15).

For completeness, we calculate also the analytic approximations of $\kappa_\pm$ by inserting Eqs. (B29) in (B29),

$$\kappa_+^{(\mathrm{AF})} = \frac{(c_0+1)}{2\zeta\left(\frac{3}{2}\right)}\left\{2\zeta\left(\frac{3}{2}\right)g' + k_1k_2T^{1/2}\left[4\pi[(c_0-1)g' + 2p] + [(c_0-1)g + 2p]\zeta\left(\frac{1}{2}\right)\zeta\left(\frac{3}{2}\right)\right]\right\} + O\left(k_1^2\right), \tag{B34}$$

$$\kappa_-^{(\mathrm{AF})} = 2(p-g') + \frac{k_1k_2T^{1/2}}{2\zeta\left(\frac{3}{2}\right)}\left\{4\pi\left[\left(c_0^2+4c_0+11\right)g' - 2p(c_0+5)\right] + \left[\left(c_0^2+4c_0+11\right)g - 2p(c_0+5)\right]\zeta\left(\frac{1}{2}\right)\zeta\left(\frac{3}{2}\right)\right\}$$
$$+ O\left(k_1^2\right). \tag{B35}$$

We can deduce from the previous equations that the analog functions $H_\pm$ for the $\kappa_\pm$ energies are dependent of the variables p and T. The system of equations for the AF phase is more complicated due to the calculation of two eigenvectors of A. Then, our approximations would be less accurate as in the previous phases (see Fig. 4). Even tough, the approximations are acceptable with the numerical calculations for $T \leqslant 0.2T_0$.

APPENDIX C: ANALYTIC APPROACH OF THE TOTAL MAGNETIZATION IN THE AF PHASE

Figure 3 indicates that the magnetization per atom M_z of the AF phase is independent of the q variable. We can prove the previous statement for low temperatures by calculating M_z with the approximate expressions found in the previous Appendix,

$$M_z = \mathrm{Tr}(\rho F_z) = \cos(2\chi)N^c + a - c$$
$$\approx p + \frac{c_0k_1k_2T^{1/2}}{(c_0+1)\zeta\left(\frac{3}{2}\right)}\left\{\zeta\left(\frac{1}{2}\right)\zeta\left(\frac{3}{2}\right)[(c_0+3)g - 2p]\right.$$
$$\left. + 4\pi[(c_0+3)g' - 2p]\right\} + O\left(k_1^2\right). \tag{C1}$$

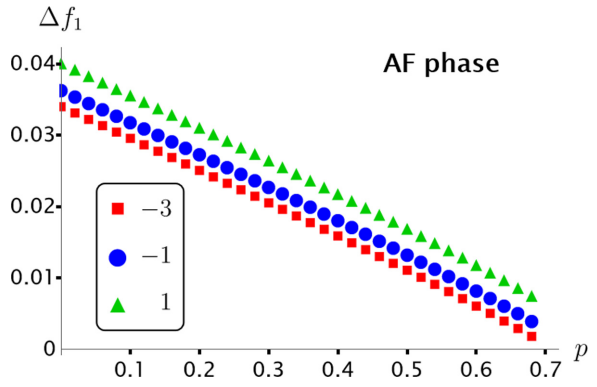

FIG. 6. The change in the fraction f_1 for the AF phase from $T = 0$ to $T = 0.2$ Δf_1 (D1) versus p for $q = -3, -1, 1$, respectively. Δf_1 decreases as one increases p. Δf_1 for $p = 0.68$ is at most 0.01.

APPENDIX D: CHANGE IN THE FRACTION f_1 FOR THE AF PHASE WITH RESPECT TO THE TEMPERATURE

In this Appendix, we summarize the numerical results regarding the change in the fraction $f_1 = \langle 1, 1| \rho |1, 1\rangle$ for the AF phase with respect to the temperature. We define

$$\Delta f_1 \equiv f_1|_{T=0.2} - f_1|_{T=0}, \tag{D1}$$

where we are using the scaled variables. Δf_1 is a function of the variables (p, q), and it is well defined only when the AF phase exists for $T = 0$ and $T = 0.2$, i.e., for $q \in [-3, 1]$ and $p \in [0, 0.68]$. We plot in Fig. 6 Δf_1 versus the p variable for $q = -3$, -1, and 1, respectively. One can conclude that the fraction f_1 is almost invariant for $p = 0.68$ in the interval of temperatures $T \in [0, 0.2]$, where Δf_1 is, at most, equal to 0.01.

[1] Y. Kawaguchi and M. Ueda, Phys. Rep. **520**, 253 (2012).
[2] C. J. Pethick and H. Smith, *Bose-Einstein Condensation in Dilute Gases* (Cambridge University Press, Cambridge, UK, 2008).
[3] M. Lewenstein, A. Sanpera, and V. Ahufinger, *Ultracold Atoms in Optical Lattices: Simulating Quantum Many-Body Systems* (Oxford University Press, Oxford, 2012).
[4] T.-L. Ho, Phys. Rev. Lett. **81**, 742 (1998).
[5] T. Ohmi and K. Machida, J. Phys. Soc. Jpn. **67**, 1822 (1998).
[6] C. V. Ciobanu, S.-K. Yip, and T.-L. Ho, Phys. Rev. A **61**, 033607 (2000).
[7] R. Barnett, A. Turner, and E. Demler, Phys. Rev. Lett. **97**, 180412 (2006).
[8] R. B. Diener and T.-L. Ho, Phys. Rev. Lett. **96**, 190405 (2006).
[9] Y. Kawaguchi and M. Ueda, Phys. Rev. A **84**, 053616 (2011).
[10] J. Stenger, S. Inouye, D. Stamper-Kurn, H.-J. Miesner, A. Chikkatur, and W. Ketterle, Nature (London) **396**, 345 (1998).
[11] D. M. Stamper-Kurn, M. R. Andrews, A. P. Chikkatur, S. Inouye, H.-J. Miesner, J. Stenger, and W. Ketterle, Phys. Rev. Lett. **80**, 2027 (1998).
[12] D. Jacob, L. Shao, V. Corre, T. Zibold, L. De Sarlo, E. Mimoun, J. Dalibard, and F. Gerbier, Phys. Rev. A **86**, 061601(R) (2012).
[13] M.-S. Chang, C. D. Hamley, M. D. Barrett, J. A. Sauer, K. M. Fortier, W. Zhang, L. You, and M. S. Chapman, Phys. Rev. Lett. **92**, 140403 (2004).
[14] S. J. Huh, K. Kim, K. Kwon, and J.-Y. Choi, Phys. Rev. Research **2**, 033471 (2020).
[15] B. D. Esry, C. H. Greene, J. P. Burke, Jr., and J. L. Bohn, Phys. Rev. Lett. **78**, 3594 (1997).
[16] H. Shi, W.-M. Zheng, and S.-T. Chui, Phys. Rev. A **61**, 063613 (2000).
[17] E. J. Mueller, T.-L. Ho, M. Ueda, and G. Baym, Phys. Rev. A **74**, 033612 (2006).
[18] M. Matuszewski, T. J. Alexander, and Y. S. Kivshar, Phys. Rev. A **78**, 023632 (2008).
[19] J. Mur-Petit, M. Guilleumas, A. Polls, A. Sanpera, M. Lewenstein, K. Bongs, and K. Sengstock, Phys. Rev. A **73**, 013629 (2006).
[20] N. T. Phuc, Y. Kawaguchi, and M. Ueda, Phys. Rev. A **88**, 043629 (2013).
[21] K. Jiménez-García, A. Invernizzi, B. Evrard, C. Frapolli, J. Dalibard, and F. Gerbier, Nat. Commun. **10**, 1 (2019).
[22] M. Sadgrove, Y. Eto, S. Sekine, H. Suzuki, and T. Hirano, J. Phys. Soc. Jpn. **82**, 094002 (2013).
[23] D. M. Stamper-Kurn, H.-J. Miesner, A. P. Chikkatur, S. Inouye, J. Stenger, and W. Ketterle, Phys. Rev. Lett. **83**, 661 (1999).
[24] H.-J. Miesner, D. M. Stamper-Kurn, J. Stenger, S. Inouye, A. P. Chikkatur, and W. Ketterle, Phys. Rev. Lett. **82**, 2228 (1999).
[25] A. Vinit, E. M. Bookjans, C. A. R. Sá de Melo, and C. Raman, Phys. Rev. Lett. **110**, 165301 (2013).
[26] N. Shitara, S. Bir, and P. B. Blakie, New J. Phys. **19**, 095003 (2017).
[27] L. M. Symes, D. Baillie, and P. B. Blakie, Phys. Rev. A **98**, 063618 (2018).
[28] J. H. Kim, D. Hong, S. Kang, and Y. Shin, Phys. Rev. A **99**, 023606 (2019).
[29] H.-X. Yang, T. Tian, Y.-B. Yang, L.-Y. Qiu, H.-Y. Liang, A.-J. Chu, C. B. Dağ, Y. Xu, Y. Liu, and L.-M. Duan, Phys. Rev. A **100**, 013622 (2019).
[30] J. Jiang, L. Zhao, M. Webb, and Y. Liu, Phys. Rev. A **90**, 023610 (2014).
[31] S. Kang, S. W. Seo, J. H. Kim, and Y. Shin, Phys. Rev. A **95**, 053638 (2017).
[32] T. Tian, H.-X. Yang, L.-Y. Qiu, H.-Y. Liang, Y.-B. Yang, Y. Xu, and L.-M. Duan, Phys. Rev. Lett. **124**, 043001 (2020).
[33] M. Heyl, Rep. Prog. Phys. **81**, 054001 (2018).
[34] J.-P. Blaizot and G. Ripka, *Quantum Theory of Finite systems* (MIT Press, Cambridge, MA, 1986).
[35] A. Griffin, T. Nikuni, and E. Zaremba, *Bose-Condensed Gases at Finite Temperatures* (Cambridge University Press, Cambridge, UK, 2009).
[36] Y. Kawaguchi, N. T. Phuc, and P. B. Blakie, Phys. Rev. A **85**, 053611 (2012).
[37] F. Gerbier, A. Widera, S. Fölling, O. Mandel, and I. Bloch, Phys. Rev. A **73**, 041602(R) (2006).
[38] E. M. Bookjans, A. Vinit, and C. Raman, Phys. Rev. Lett. **107**, 195306 (2011).
[39] C. Samuelis, E. Tiesinga, T. Laue, M. Elbs, H. Knöckel, and E. Tiemann, Phys. Rev. A **63**, 012710 (2000).

[40] I. Bengtsson and K. Życzkowski, *Geometry of Quantum States: An Introduction to Quantum Entanglement*, 2nd ed. (Cambridge University Press, Cambridge, UK, 2017).
[41] H. Mäkelä and K.-A. Suominen, Phys. Rev. Lett. **99**, 190408 (2007).
[42] The influence of the temperature on the phase diagram for spinor condensates have been previously investigated theoretically [35,36,50–52] and experimentally [49,53–55].
[43] A. Griffin, Phys. Rev. B **53**, 9341 (1996).
[44] N. P. Proukakis and B. Jackson, J. Phys. B: At., Mol. Opt. Phys. **41**, 203002 (2008).
[45] N. T. Phuc, Y. Kawaguchi, and M. Ueda, Phys. Rev. A **84**, 043645 (2011).
[46] E. Majorana, Nuovo Cimento **9**, 43 (1932).
[47] E. Serrano-Ensástiga and D. Braun, Phys. Rev. A **101**, 022332 (2020).
[48] The numerical solutions for $T = 0$ were calculated as the limit $T \to 0$, considering the values $T = 10^{-n}T_0$ with $n = 3, \ldots, 6$.
[49] C. Frapolli, T. Zibold, A. Invernizzi, K. Jiménez-García, J. Dalibard, and F. Gerbier, Phys. Rev. Lett. **119**, 050404 (2017).
[50] G. Lang and E. Witkowska, Phys. Rev. A **90**, 043609 (2014).
[51] W. Zhang, S. Yi, and L. You, Phys. Rev. A **70**, 043611 (2004).
[52] N. T. Phuc, Y. Kawaguchi, and M. Ueda, Ann. Phys. **328**, 158 (2013).
[53] M. Erhard, H. Schmaljohann, J. Kronjäger, K. Bongs, and K. Sengstock, Phys. Rev. A **70**, 031602(R) (2004).
[54] H. K. Pechkis, J. P. Wrubel, A. Schwettmann, P. F. Griffin, R. Barnett, E. Tiesinga, and P. D. Lett, Phys. Rev. Lett. **111**, 025301 (2013).
[55] X. He, B. Zhu, X. Li, F. Wang, Z.-F. Xu, and D. Wang, Phys. Rev. A **91**, 033635 (2015).